International Journal of Applied Earth Observation and Geoinformation 43 (2015) 102–118

Contents lists available at ScienceDirect

International Journal of Applied Earth Observation and Geoinformation

journal homepage: www.elsevier.com/locate/jag

Observing system simulations for small satellite formations estimating bidirectional reflectance

Sreeja Nag[a,b,*], Charles K. Gatebe[b,c], Olivier de Weck[a]

[a] Massachusetts Institute of Technology, Cambridge, MA 02139, USA
[b] NASA Goddard Space Flight Center, Greenbelt, MD 20771, USA
[c] Universities Space Research Association, Columbia, MD 21046, USA

ARTICLE INFO

Article history:
Received 1 November 2014
Accepted 30 April 2015
Available online 4 September 2015

Keywords:
Multi-angular remote sensing
Small satellite
Formation
BRDF
OSSE

ABSTRACT

The bidirectional reflectance distribution function (BRDF) gives the reflectance of a target as a function of illumination geometry and viewing geometry, hence carries information about the anisotropy of the surface. BRDF is needed in remote sensing for the correction of view and illumination angle effects (for example in image standardization and mosaicing), for deriving albedo, for land cover classification, for cloud detection, for atmospheric correction, and other applications. However, current spaceborne instruments provide sparse angular sampling of BRDF and airborne instruments are limited in the spatial and temporal coverage. To fill the gaps in angular coverage within spatial, spectral and temporal requirements, we propose a new measurement technique: use of small satellites in formation flight, each satellite with a VNIR (visible and near infrared) imaging spectrometer, to make multi-spectral, near-simultaneous measurements of every ground spot in the swath at multiple angles. This paper describes an observing system simulation experiment (OSSE) to evaluate the proposed concept and select the optimal formation architecture that minimizes BRDF uncertainties. The variables of the OSSE are identified; number of satellites, measurement spread in the view zenith and relative azimuth with respect to solar plane, solar zenith angle, BRDF models and wavelength of reflection. Analyzing the sensitivity of BRDF estimation errors to the variables allow simplification of the OSSE, to enable its use to rapidly evaluate formation architectures. A 6-satellite formation is shown to produce lower BRDF estimation errors, purely in terms of angular sampling as evaluated by the OSSE, than a single spacecraft with 9 forward-aft sensors. We demonstrate the ability to use OSSEs to design small satellite formations as complements to flagship mission data. The formations can fill angular sampling gaps and enable better BRDF products than currently possible.

1. Introduction

Multi-angular remote sensing, or sensing of the same target at multiple angles, is very important for obtaining various science products such as albedo, for land cover classification, for cloud detection, and for atmospheric correction (Gatebe et al., 2003). Sparse angular sampling of the reflected light can cause errors between 15% and 90% in the reflectance products of moderate resolution, solar wavelength remote sensing (Esper et al., 2000; Nag, 2015). Up to 90% of the errors in the computation of radiative forcing, a key assessor of climate change, is attributed to the lack of detailed description of reflected solar flux (Wielicki and Harrison, 1995). Total Outgoing Radiation (TOR) is estimated at 0.9 W/m^2 by current climate models—with uncertainties of −2 to +7 W/m^2 (Loeb et al., 2009), reduced only by frequent, global, angular radiance measurements (Dyrud et al., 2014). Snow albedo when estimated using only nadir reflectance shows up to 45–50% errors compared to hemispherical reflectance (Arnold et al., 2002). Current Gross Primary Productivity (GPP) estimates show uncertainties up to 40% in the terrestrial carbon uptake (Hilker et al., 2011). Vegetation analysis is adversely affected by under-sampling on the principal plane and hotspots (Román et al., 2011). GPP and vegetation reflectance quantifies the extent to which forests and vegetation act as a sink for atmospheric carbon dioxide and is very important to estimate carbon feedbacks of vegetation in response to global climate change (Canadell et al., 2007). Deforestation and forest degradation accounts for 12% of anthropogenic carbon emissions, which have nearly doubled in the past 30 years (Van der Werf et al., 2009). Recent studies have also shown an overestimation

* Corresponding author at: Bay Area Environmental Research Institute, Sonoma, CA 95476, USA.
E-mail address: sreejanag@alum.mit.edu (S. Nag).

http://dx.doi.org/10.1016/j.jag.2015.04.022
0303-2434/

of the greening of Amazon forests during the dry season due to seasonal artifacts in MODIS' sun-sensor geometry (Morton et al., 2014). Using denser, space-based angular sampling from the CHRIS instrument (Barducci et al., 2005) reduces GPP uncertainties to 10% (Hall et al., 2008), showing a 75% improvement in carbon cycle calculations. The above shortcomings will not disappear but can be significantly improved by better angular sampling of the BRDF function.

This paper proposes a new measurement solution for multi-angular remote sensing and details the observing system simulation experiment (OSSE) designed to optimize the solution, with the goal of selecting a few optimal mission designs. The measurement solution is intended to complement current flagship and Decadal Survey missions, by alleviating some sampling requirements that could cause creeps. The Earth Science Decadal Survey asked for "*Synergies of complementary measurements...cost-effective replacement of individual sensors... moving away from a single parameter and sensor-centric approach toward a systems approach that ties observations together to study processes important to understanding Earth-system feedbacks*" when proposing 15 instruments for the next decade (National Academy of Sciences, 2007). Seven years later, only 3 of those are in formulation, causing the Survey's mid-term assessment to stress on complementary solutions like hosted payloads and formation flight (National Research Council, 2012). The proposed solution in this paper seeks to do the same, by identifying a quantifiable gap in Earth remote sensing and addressing it using small satellite formations.

The presented OSSE is a subset of a larger evaluation framework, which generates and evaluates the engineering design tradespace of solutions. The models within the OSSE have been carefully evaluated in the context of space-based measurements by formations and the surface types expected to be sampled over time. Reference data are designated from a combination of airborne and spaceborne data collected during NASA campaigns and validated using radiative transfer models. The design, nature and validation of the OSSE are indispensable to the selection of the optimal measurement solution owing to the complexity of distributed missions. A baseline design has been proposed in the case study, and its multi-angular advantages to other candidate designs and over a monolithic counterpart demonstrated using the developed OSSE.

1.1. Why Bi-directional reflectance?

The bidirectional reflectance distribution function (BRDF) gives the reflectance of a target as a function of illumination geometry and viewing geometry, hence carries information about the anisotropy of the surface (Gatebe et al., 2003). BRDF itself, as a ratio of infinitesimals, is a derivative with instantaneous values of reflected radiance and solar illumination (Nicodemus et al., 1977). BRDF is influenced by intrinsic properties of the reflecting surface that can be measured within the surface itself without any reference to a larger space. While it can never be measured directly, real measurements can involve non-zero intervals of above parameters. It depends on four major angles—the solar zenith angle or SZA, solar azimuth angle, view zenith angle or VZA and view azimuth angle—as well as on the wavelength of light (Gatebe et al., 2003). The azimuth angles are added to provide one azimuth angle relative to the solar position called the relative azimuth angle or RAA. Estimating BRDF (Barnsley et al., 1994) requires radiance measurements across a large angular spread, with spectral range over the visible and near infrared (VNIR) solar spectrum and with spatial resolution that is appropriate for sampling BRDF of surface types of interest. Frequent temporal measurements can allow monitoring of regions of interest, and allow global coverage. To name a few applications, BRDF is used for the derivation of surface albedo (Lyapustin et al., 2010), calculation of radiative forcing (Liang, 2008), land cover classification (Privette et al., 1997), gross primary productivity (Hilker et al., 2008), cloud detection (Esper et al., 2000), surface roughness measurements of vegetation, snow or ice (Gatebe et al., 2003; Chopping, 2008), canopy structure (Chopping, 2008; Chopping et al., 2008), atmospheric corrections, and aerosol optical properties (Gatebe et al., 2003).

1.2. Gaps in current measurements

Current measurement techniques are inadequate for estimating global BRDF. Spacecraft instruments approximate BRDF by making multi-angular measurements owing to their large cross-track swath (e.g. Moderate Resolution Imaging Spectroradiometer-MODIS (Xiong et al., 2011), now retired Polarization and Directionality of the Earth's Reflectances-POLDER (Deschamps et al., 1994), Clouds and Earth's Radiant Energy System-CERES (Wielicki et al., 1996), multiple forward and aft sensors (e.g. Multi-angle Imaging SpectroRadiometer-MISR (Diner et al., 1998), Along Track Scanning Radiometer-ATSR (Godsalve, 1995), Advanced Spaceborne Thermal Emission and Reflection Radiometer-ASTER (Abrams, 2000), or autonomous maneuverability to point at pre-programmed ground targets (e.g. Compact High Resolution Imaging Spectrometer -CHRIS (Barducci et al., 2005).

Since angular sampling requires simultaneous reflectance measurements at multiple angles for a given ground footprint, one satellite is insufficient for accurate characterization. A single large, complex satellite (monolith), especially a forward-aft or cross-track sensors in sun synchronous orbits (SSO) such as MISR or MODIS, can make measurements only along a restrictive plane with respect to the solar phase because SSOs have nearly constant beta angles and local crossing times. Angular reflectance acquisition by monoliths typically combines measurements along-track if they have forward-aft sensors (Fig. 1-left) or cross-crack if they have a large swath (Fig. 1-right). Measurements made by cross-track sensors are separated in time by more than a week (e.g. MODIS, CERES). In areas of fast changing surface/cloud conditions especially during the melt season/tropical storms, a few days can make a big difference in reflectance. The three shown look angles in Fig. 1 are only examples. In reality, many such measurements are combined.

Spaceborne instruments that provide good angular sampling compromise in other sampling characteristics. Table 1 compares seven spaceborne instruments with BRDF-dependent products in terms of angular sampling (Col #1), spatial resolution (Col #2), temporal resolution (Col #3) and spectral range and resolution (Col #4 and #5). The number of angles indicate near simultaneous angular measurements of the same ground spot and RGT is the repeat ground track period. Since our proposed measurement solution is expected to make near-simultaneous angular measurements, the time of acquisition in Table 1 is restricted to a few minutes to make a fair comparison. POLDER, MISR and CHRIS provide many angular measurements, but POLDER has very coarse ground resolution, CHRIS has no target repeatability for temporal monitoring of surface types and MISR is restricted to only four bands in VNIR and to near-constant solar phase. MODIS and CERES are cross-track sensors so they get only one view at one angle every orbit, of the same ground spot. ATSR and ASTER, with their double cameras, are able to scale this up to two angles every orbit. However, their long repeat period and narrow swath, respectively, limit how quickly they can accumulate good sampling.

Airborne instruments can provide dense angular, spectral sampling at fine spatial resolution but it is very expensive to make frequent, repeated measurements globally. NASA GSFC's heritage airborne BRDF instrument, the Cloud Absorption Radiometer (CAR) (King et al., 1986), has 14 channels and can make up to 114.600 directional measurements of radiance per channel per aircraft circle at a spatial resolution of 10–270 m (Gatebe et al., 2003). CAR's

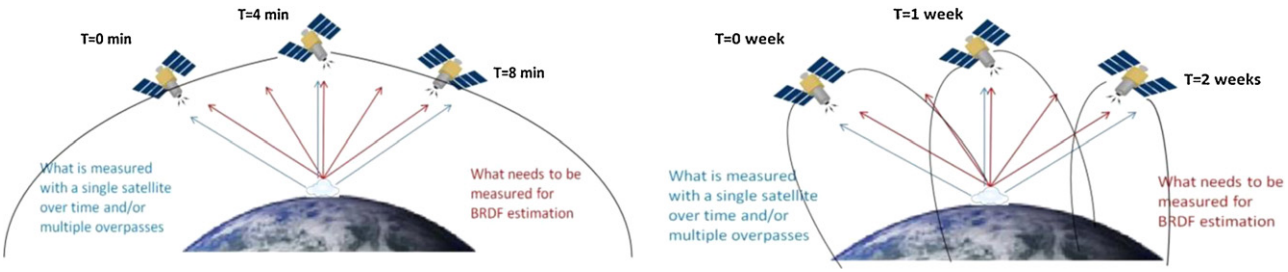

Fig. 1. Measurements a single satellite is capable of making over time, in blue, versus instantaneous angular sampling required for BRDF estimation, in red. 'T', ranging over a few minutes for forward-aft sensors in the left panel or over a couple of weeks for cross-track sensors in the right panel, represents nominal time differences that a LEO satellite takes to make the given blue measurements.(For interpretation of the references to colour in this figure legend, the reader is referred to the web version of this article.).

Table 1
Comparison of current spaceborne instruments with BRDF products (rows) in terms of BRDF measurement metrics (columns). Red highlights indicate sparse measurements for BRDF estimation. The instrument acronyms have been defined in the text. The superscripted numbers indicate cross-track (1), along-track (2) and autonomously manoeuvred (3) viewing geometry.

Science metrics → ↓Current instruments	Number of angles	Ground pixel size in km X km	Revist time (any view) in days	Spectral range	# of spectral bands
1MODIS	1	0.25 to 1	~2(16 day RGT)	0.4–14.4 μm	36
1POLDER	12	6 × 7	~2(16 day RGT)	0.42–0.9 μm	9
1CERES	1	10 to 20	~2(16 day RGT)	0.3–12 μm	3
2MISR	9	0.275 to 1.1	9(16 day RGT)	0.44–0.87 μm	4
2ATSR	2	1 to 2	3–4	0.55–12 μm	7
2ASTER	2	0.015 to 0.09	~2(16 day RGT)	0.52–11.65 μm	14
3CHRIS	5–15	0.017 to 0.5	As per command	0.415–1.05 μm	18–63

estimated BRDF can improve the local surface albedo errors by 15–20% when compared to MODIS-derived BRDF (Gatebe et al., 2014). However, it loses out on global coverage that MODIS offers because CAR campaigns are local and observations usually span several weeks during a field campaign.

Given the importance of BRDF and its science products (Canadell et al., 2007), it is important to design and develop an alternative observational system that combines the local accuracy of airborne instruments with the global coverage and frequent and repeated measurements of spaceborne instruments. Based on the CAR instrument BRDF angular sampling strategy (National Research Council, 2012; Yost, 2013), which is assumed here as a golden standard and MISR's angular spread, we attempt to determine an optimum angular spread for a global BRDF sampling using small satellites. MISR is chosen as the monolithic reference because of its best angular performance in Table 1, while being global with moderate spatial resolution. Spatial requirements can be set at 350 m at 865 nm, as compared to MISR's 275 m. These tentative requirements are shown to be achievable using small satellite technology within signal-to-noise ratio of 50 (Nag, 2015; Nag et al., 2013).

1.3. Proposed measurement solution

Previous literature has proposed the use of a satellite formation to complement the deficiency of a monolithic system for multi-angular measurements and BRDF estimation (King et al., 1986; Gatebe et al., 2014; Nag, 2015). A formation or cluster is defined as a satellite constellation where the satellites have a specific spatial or angular arrangement among themselves, and are continuously able to "see" each other. The formation would have small satellites (10–20 kg) in repeating-ground-track formation flight carrying spectrometer payloads to make multi-spectral measurements over a ground spot, at multiple angles at the same time (Fig. 2). One satellite would point nadir, while the others would point their payload toward the ground spot of the nadir-pointing satellite. Many small satellites can be deployed with the same resources required for a single current large monolith. The 6U to 12U CubeSat standards can be used as the bus and NASA's ELANA Program for launch opportunities (Skrobot and Coelho, 2012). For adequate spatial and spectral sampling, small VNIR imaging spectrometers can be configured for snapshot imaging to maximize ground spot overlap (Nag et al., 2013). Baseline formation designs have been shown to be feasible within currently available technologies (Nag, 2015).

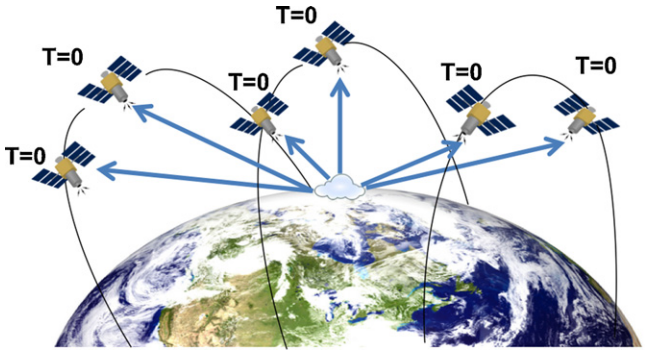

Fig. 2. A satellite formation making multi-angular, multi-spectral measurements by pointing its spectrometers at the same ground spot, as it orbits the Earth (not to scale).

A simplified but reliable OSSE is needed to map the generated engineering designs with BRDF estimation improvement, so that designs that optimize performance and cost can be selected. Such a small satellite formation cannot outperform monoliths in all the metrics in Table 1, due to the constraints of its size, mass and available technology. For example, small satellites are currently far less

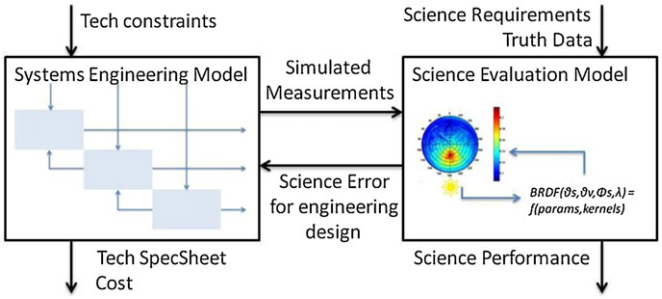

Fig. 3. Tradespace analysis tool overview. OSSE-based science evaluation (right box) is tightly coupled to the traditional MBSE module (left box).

optimal in radiometric accuracy or image stability than the current monolithic flagship missions. However, we argue that their value lies not in competition but in being able to provide complementary data that when used with flagship mission can produce BRDF or other dependent Earth science products that would be impossible otherwise.

2. Observing system simulation approach

An architecture is defined as a unique combination of design variables such as number of satellites, their orbit parameters, spectrometer payload's field of view, imaging mode, etc. The methodology employed to assess the optimal architectures and validate their BRDF estimation capabilities couples Model-Based Systems Engineering (MBSE) with Observing System Simulation Experiments (OSSE) (Nag, 2015; Nag et al., 2014). A tradespace of architectures can be analyzed by varying the design variables in the MBSE model and assessing its effect on data assimilation and science products using OSSEs, as shown in Fig. 3. The left hand box generates architectures (Nag et al., 2013, 2015a), sizes them to check their feasibility and costs them in keeping with the MBSE approach. The model can be simulated over any time horizon, divided into appropriate time steps. The focus of this paper is the right hand box, which evaluates science performance.

The method to build a reliable OSSE has been developed based on literature on OSSEs through their historical development (Arnold and Dey, 1986) and for CLARREO (Feldman et al., 2011), HyspIRI (Turmon et al., 2010) and the Hydros Radiometer (Crow et al., 2005). Section 3 details the data and models used in the OSSE for BRDF estimation and Section 4 analyses the sensitivity of performance with respect to key variables in BRDF estimation. OSSEs are extremely expensive computationally (Feldman et al., 2011). Sensitivity studies allow us to streamline our OSSE variable space so that a simplified OSSE can be used for rapid architecture studies in a mission's pre-Phase A instead of the traditional, complex, instrument validation. All models described in this paper have been built on MATLAB 2014a or AGI's Satellite Tool Kit[1] (STK). Orbits are simulated and propagated on STK's High Precision Propagator (HPOP), its inputs customized for rapid architecture generation and outputs customized for angular analysis and feed-forward into the OSSE (Nag et al., 2015a). Section 4 shows the performance-cost trades of hundreds of architectures of formations using the streamlined OSSE to calculate performance, in conjunction with parallel literature to generate architectures (Nag et al., 2015a) and calculate costs (Nag, 2015).

The science evaluation model (Fig. 4) is driven by observing system simulation experiments or OSSEs. Inputs to the model are the solar zenith angle (SZA), view zenith angle (VZA) and relative azimuth angle (RAA) of all satellites in a formation at any given instant of time, which comes from the systems engineering model, and the surface of interest, which is an external requirement. The reference BRDF data used in the model (Box1 in Fig. 4) are reflectance measurements made by the CAR at every degree of VZA and RAA for seven representative surface types. The surface type under the satellite looking nadir is identified using the satellite's position and attitude from the systems engineering model and a MODIS database of globally gridded surface types.[2] While BRDF is known to vary within the same surface type, we assume that the variance of gross features or patterns is less than that between the seven surface types. Availability of more intricate global maps of terrains and dense angular reflectance data at those terrains can be used to refine the reference data and improve the OSSE's accuracy.

A sample of this Reference BRDF (Box3) corresponding to what each satellite senses and depending on its position and attitude at every time step (Box2 from MBSE output), is used as data to invert a BRDF model (Box4) and estimate the model parameters. These parameters are then used to run the forward model and calculate reflectance at every degree of VZA and RAA, given an SZA (Box6). The difference between this estimated reflectance and the reference CAR reflectance is called the BRDF; and is represented as a Root Mean Square value (RMS). BRDF can then be used to calculate albedo, GPP or any other BRDF-dependent product (Nag, 2015). The difference between these products calculated from the CAR reflectance values versus the forward model estimated reflectance values form the App Error. These errors at any time step are the outputs from the science performance evaluation model and determine the goodness of the input formation design and corresponding angular spread. The error over time for a full tradespace of formation architectures is used as a science metric to judge the performance of the cluster. These errors can be traded against the cost of increasing the number/size of satellites and complexity of the formation for making value-centric decisions in engineering design. Alternative performance metrics that may be used in the OSSE are noise amplification factors (WOD, weight of determination) which quantifies the uncertainty in retrieved parameters such as nadir-view reflectance, albedo at various solar zenith angles or BRDF model parameters (Lucht and Lewis, 2000).

2.1. Reference BRDF data

Airborne or tower data of multi-angular reflectance serve as reference reflectance data for the science evaluation model. For some OSSEs such as those for estimating total outgoing radiation globally, exhaustive measurements are not available hence, radiative transfer model simulations are used to fill up the gaps. As mentioned before, local BRDF data from CAR's airborne campaigns on platforms such as NASA P-3B is used as reference (Gatebe et al., 2003). The CAR is designed to have a zenith to nadir scan range of 190°. By flying it around a ground spot in circles and at different heights, radiance measurements are obtained at every degree of zenith and azimuth angle to provide a very dense angular sampling of BRDF (Gatebe et al., 2003). By repeating measurements at different times of the day, reflectance at different solar zenith angles may also be available.

CAR data for all seven major surface types are available. Fig. 5 shows the global distribution of the surface types, as extracted from

[1] Analytical Graphics Inc. website and products: http://www.agi.com/products/stk/.

[2] Global Land Cover Facility Website (GLCF): http://glcf.umd.edu/data/lc/. Data extracted by and used with permission from Gong Zhang at NASA Ames Research Center.

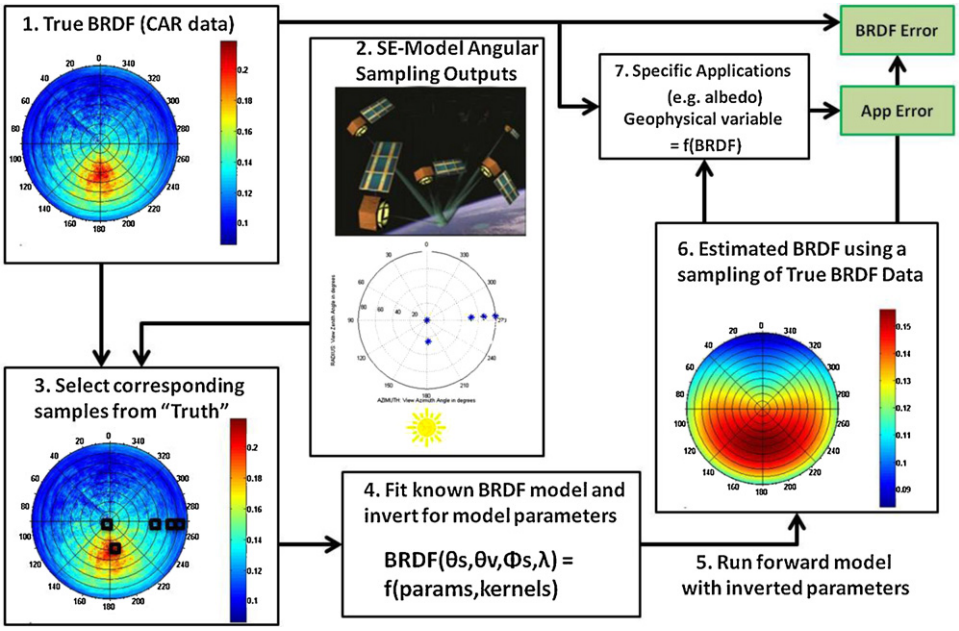

Fig. 4. Science evaluation model driven by OSSE. The model uses angular output from the formation architectures in the systems engineering model (Box2) to simulate the fraction (Box3) of the reference data (Box1) as "seen" by the formation. The metrics of performance, BRDF error and application "App" error (green boxes), are calculated by estimating BRDF (Box5) using science models (Box4) on the "seen" fraction.

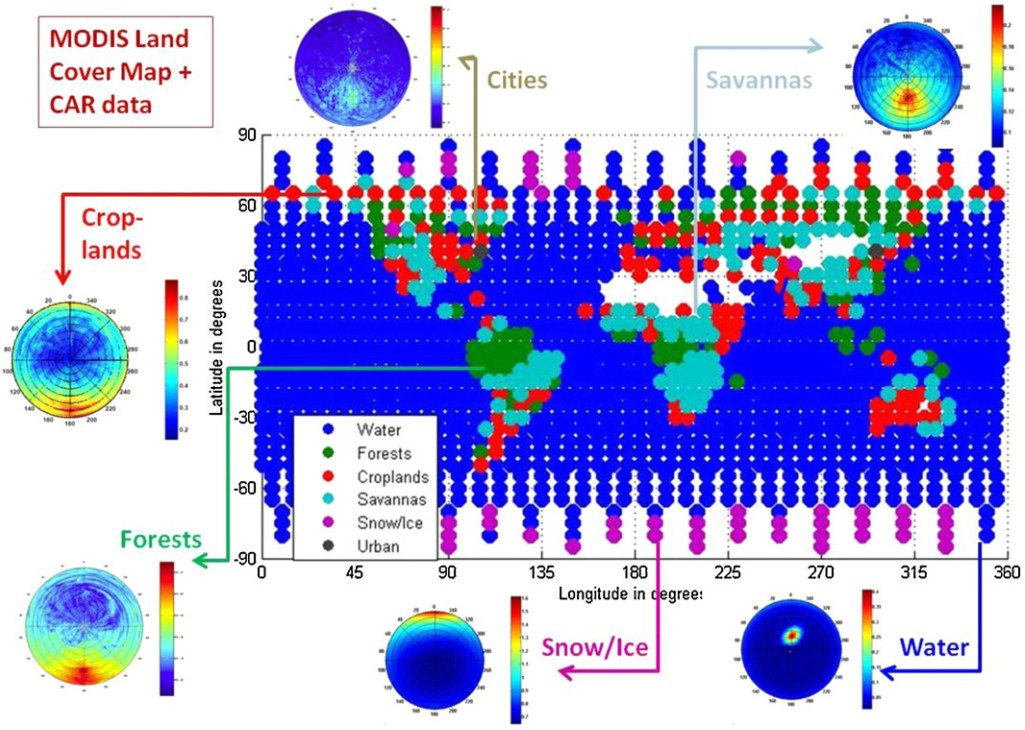

Fig. 5. Typical BRDF,at representative wavelengths (see text for values), of the major BRDF surface types, geographically sorted using the MODIS land cover type. The white gaps indicate deserts.

the Global Land Cover Facility (GLCF) which draws from MODIS data. The grid points are 5° apart at the equator and distance-adjusted for higher latitudes. For each surface type, the inset polar plots show the reflectance normalized at the top of the atmosphere as a function of measurement zenith (plot radius) and azimuth with respect to the Sun (polar azimuth). Both the shape and the intensity values of these plots are very different, indicating the importance of local but angular data collection as well as global and temporal assessment of this data.

NASA CLAMS campaign (2001) data from Virginia Beach has been used as water BRDF reference data (Gatebe et al., 2005). The inset in Fig. 5 shows the data at SZA = 20°. Three other data sets at SZA = 16°, 30° and 44° have been shown in more detail in Fig. 4. Quite obviously, water BRDF is characterized by a reflectance peak

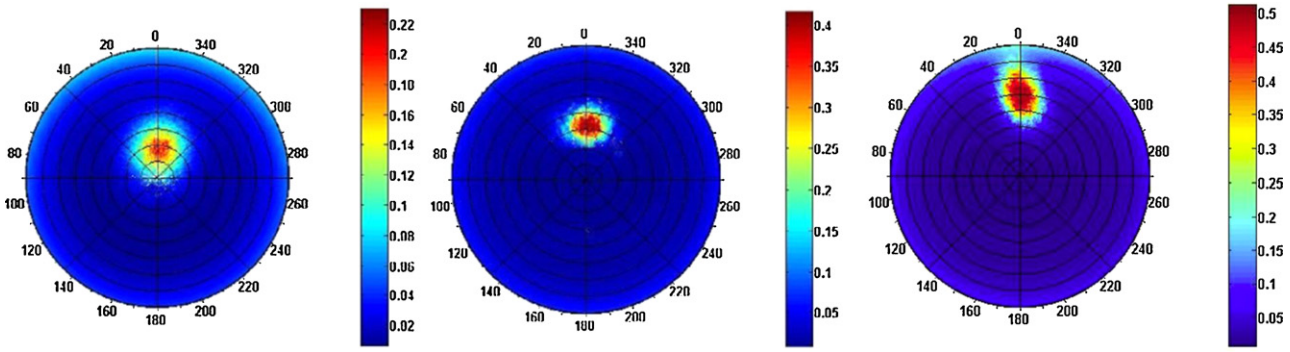

Fig. 6. BRDF sample of water as collected off Virginia Beach by the CAR instrument during NASA's CLAMS campaign, 2001. Reflectance at solar zenith angle of 16°, 30° and 44° (left to right) is shown. The radial striations for all the data plots are 10° in view zenith angle (VZA).

for the sun glint or specular reflectance when view zenith and solar zenith angles as well as both azimuths (RAA = 0) are equal. While angular reflectance around the sun glint can provide valuable information about wind speeds and aerosols, the regions far from the sun glint are very important for the ocean color community (Gatebe et al., 2005). Satellite formations can be optimally arranged to measure or avoid the sun glint depending on the application of interest. Reflectance at 472 nm has been plotted and used, because the blue band (among CAR's 8 available bands) shows the ocean anisotropy more clearly and can be used successfully for ocean color retrievals (Gatebe et al., 2005).

Data collected during the SAFARI campaign (2000) in southern Africa is used for Savannah vegetation (Gatebe et al., 2003). The savannah is characterized by a distinct backscattering peak in the principal plane (RAA = 180°) called the hot spot, around the angular point where SZA = MZA. The hotspot region is very useful quantifying photosynthetic productivity. The inset in Fig. 5 shows the data collected over Skukuza, South Africa, at SZA = 28° (Gatebe et al., 2003) and expanded in Fig. 7. Savannah data at SZA = 67°, as collected from Maun in Botswana, shows the re-positioning of the hotspot as SZA changes (Gatebe et al., 2003). Both plots show reflectance at the red band (682 nm). In the absence of the green band in CAR, the redband's BRDF is used as reference because it correlates very strongly with green band BRDF obtained from tower measurements (Nag, 2015) and captures savannah anisotropy well.

Snow measurements are obtained from the ARCTAS campaign (2008) (Lyapustin et al., 2010), in Alaska. Fig. 7 (rightmost) shows the BRDF pattern at the near infrared band of 1036 nm, the chosen band for snow because of its minimal obstruction due to cloud cover and aerosols. The SZA is 66° and the specular reflectance direction shows the distinct sun glint, which is characteristic of snow, however much more diffused than the one seen over water. The BRDF patterns over forests and croplands (Fig. 3) are very similar to the ones over savannah. The insets show the BRDF pattern at 870 nm for forests, collected during the Eco3D campaign out of NASA Wallops Flight Facility, Virginia in 2011, and for croplands, collected during the CLASIC Campaign out of Ponca City, Oklahoma in 2007. The band was chosen because the surface anisotropy was observed to be the most pronounced among the NIR bands and need to be captured by the formation flight solution. Desert surfaces are often characterized by predominant forward scattering, but the reflection function is very smooth elsewhere as shown in (Soulen et al., 2000). The hemispheric albedo of the desert is less than 13% compared to the nadir albedo in contrast to 45–50% difference observed for snow (Arnold et al., 2002). The angular sampling requirements are thus less stringent for deserts compared to the other surface types defined in this study.

The satellite positions over every timestep from the systems engineering model inform which surface type lies under the nadir-pointing satellite of the formation, and the appropriate reference data is used in the OSSE. The global grid sampling is coarser than the spectrometer ground spot, hence, only one surface type per time step is processed. The position of the monolithic spacecraft such as TERRA or PARASOL is obtained from their Two Line Elements (TLE) database within AGI STK. Exact orbital states for formations of individual satellites can be used to determine angular spread (Nag et al, 2015a), which is then evaluated in the OSSE. Note that the radial striations for all the data plots (Fig. 6 through Fig. 11) are 10° in VZA.

2.2. BRDF models

BRDF models are used to estimate reflectance values at all combinations of view zenith, solar zenith and relative azimuth angle as a function of those angles and various parameters. These models may be classified in a number of ways (Shell, 2004), such as those based upon the treatment of the optics and others being physical or empirical. Physical models rely upon first-principle physics of electromagnetic energy and material interactions, and require inputs such as surface roughness parameters and the complex index of refraction. Empirical models rely solely upon measured BRDF values, while semi-empirical models incorporate some measured data, but may have significant elements of physics-based principles. For this study, semi-empirical models will be used to model BRDF as a function of 4 angles and wavelength. The most popular models for BRDF estimation are the Ross-Thick Li-Sparse (RTLS) model (Wanner et al., 1995; Roman et al., 2012; Román et al., 2011), Rahman-Pinty- Verstraete (RPV) model (Rahman et al., 1993; Martonchik et al., 1998), modified RPV to remove the non-linear terms in the RPV model and Cox-Munk model (CM) (Cox and Munk, 1954; Gatebe et al., 2005). RPV models have been applied for BRDF retrievals using MISR data, RTLS for MODIS data and CM for directional ocean reflectance (Gatebe et al., 2005).

The RTLS model is the most linear of the three. It is a linear sum of 3 kernels, dependent on the 3 BRDF angles, and a simple inversion of 3 parameters is required. The RPV formulation splits a BRF field into a scalar amplitude component and the associated angular field describing the anisotropy of the surface. The RPV model can be linearized by modeling BRDF in its logarithmic form and the linear equation (called modified RPV or MRPV) then reduces to a weighted sum of 3 kernels. Cox-Munk model is the most non-linear among the mentioned 3 models and simulates the reflectance of the wind-ruffled ocean surface outside the glitter. In our formulation, the parameters for non-linear inversion are wind speed (v), aerosol optical depth ($\tau 0$) and the path radiances. The latter is dependent on the first two variables through the full radiative transfer model, but will be assumed constant in this paper (Gatebe et al., 2005).

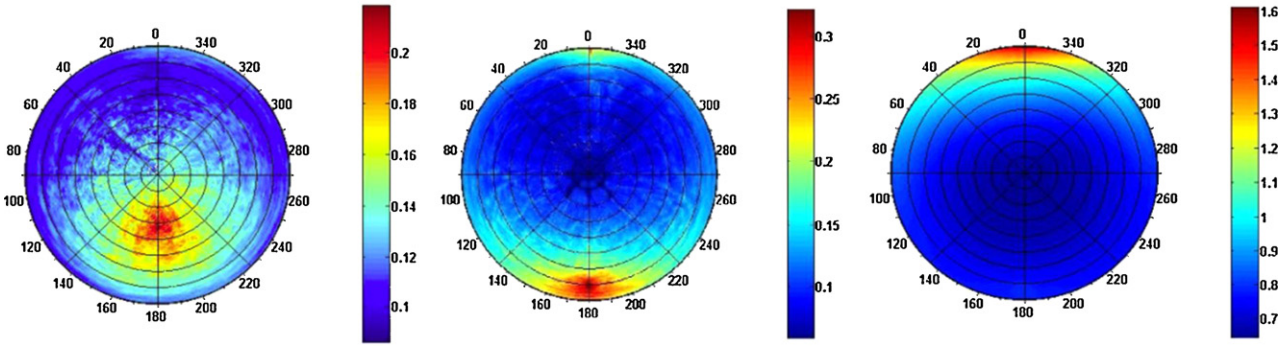

Fig. 7. NIR BRDF sample of savannah (left, middle) as collected over Maun, Botswana (left) and Skukuza, South Africa (middle) by the CAR instrument during NASA's SAFARI campaign, 2000. Reflectance shown is at solar zenith angle 28° and 67° respectively. NIR BRDF sample of snow (right) over Alaska during the ARCTAS campaign in 2008 is shown for solar zenith angle 66°.

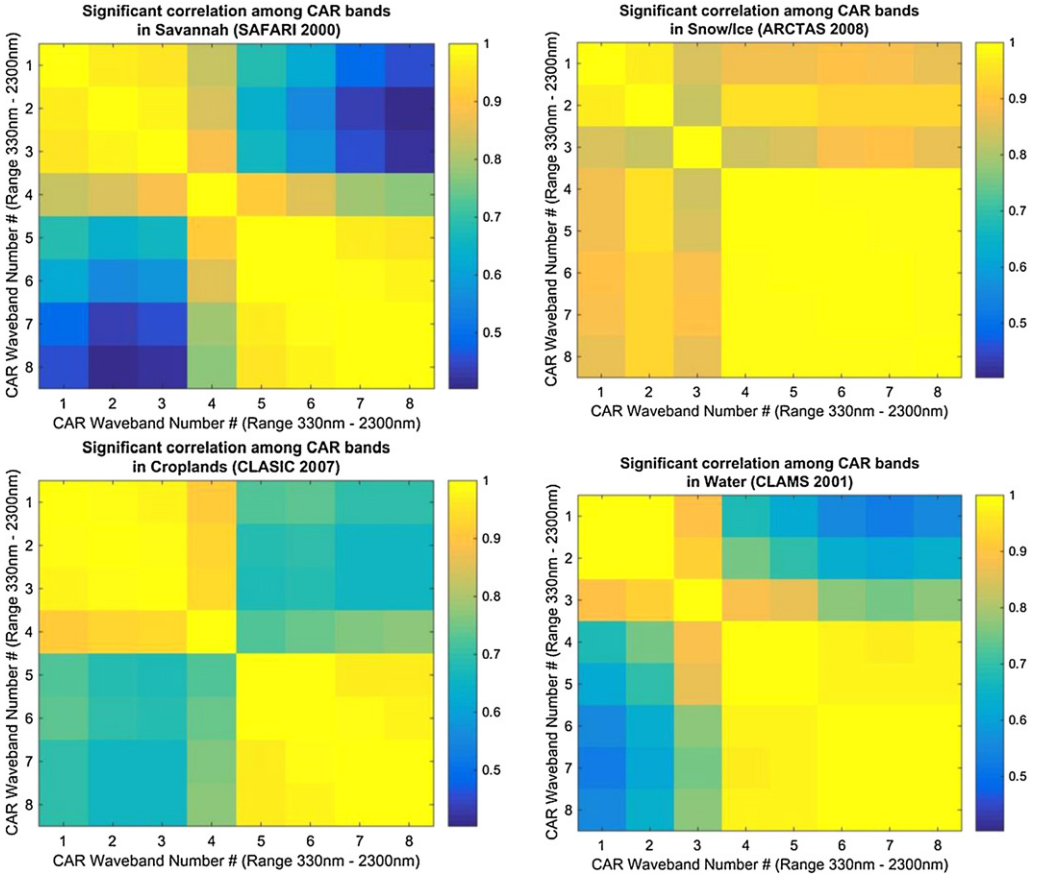

Fig. 8. Correlation at p value < 0.05 among data collected by CAR at 8 different wavebands, taken two at a time, for 4 of the 7 major surface type.

2.3. Optimization methods for angular sampling

Heuristic optimization is used to find the optimal measurement spread in the VZA–RAA plane for a given satellite number and CAR data set (per surface type). These optimal spreads are practically not precisely possible to achieve or maintain because any measurement configuration in space is constrained by possible orbits and dynamically changes as the satellites move relative to each other. However, these optimal spreads can inform us of what the ideal measurement should be. BRDF estimation dependence on SZA (decoupled due to reference data constraints) and satellite number will be analyzed in the subsequent sections.

Our approach is to optimize the position of N points on the polar plot of BRDF data (constant SZA), i.e. Box 3 in Fig. 4, such that BRDF error is minimized, i.e. green box in Fig. 4. N points correspond to the measurements taken by a formation of N satellites. The problem is very nonlinear because the objective function – BRDF error – depends non-linearly on the variable space – N-fold VZA, N-fold RAA, both for RTLS and CM models. The CM models are even more complex because their inversion process is non-linear as well.

MATLAB-based simulated annealing (SA) was selected as the algorithm of choice after testing the available options (De Weck et al., 2008) on the snow data set with $N = 5$ measurements (Nag, 2015). Gradient search algorithms or other local methods fail to optimize the space. Pattern search optimization, local but applicable to functions that are not continuous or differentiable, converges to an acceptable but non-optimal solution. Evolutionary algorithms perform equally well in the task, however with differing speeds and

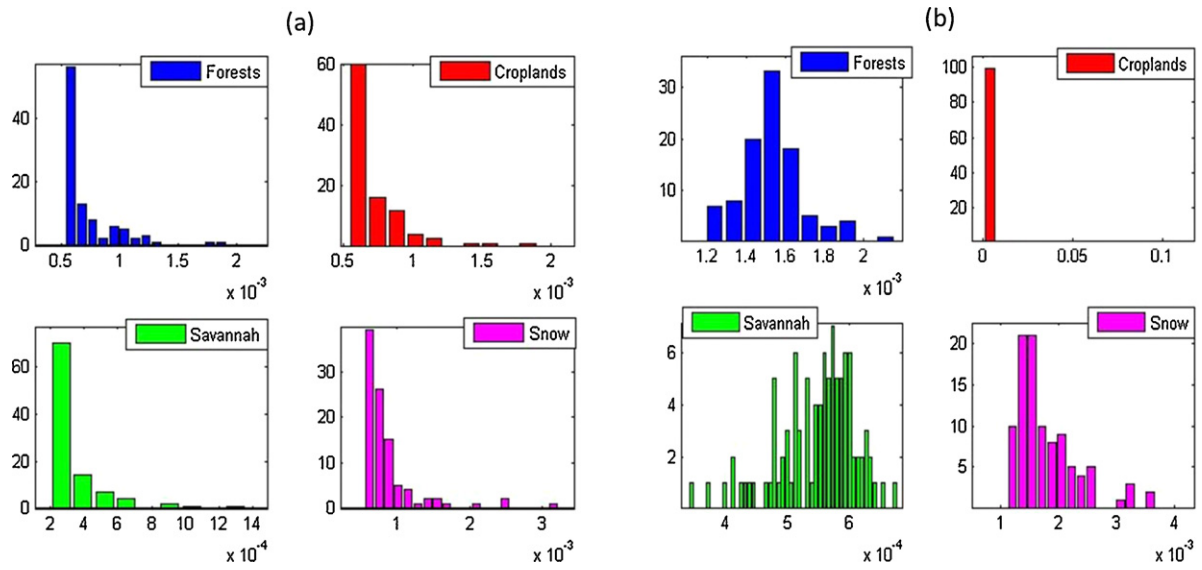

Fig. 9. Histograms of BRDF RMS errors (*X*-axis) over 100 Monte Carlo runs for four different land surface types when using the (a) RTLS or (b) modified RPV model as the model of choice in Box 4 of Fig. 4. The *X*-axis has not been normalized to the same scale because the data is not as well visualized due to the difference in absolute values of error among different surfaces.

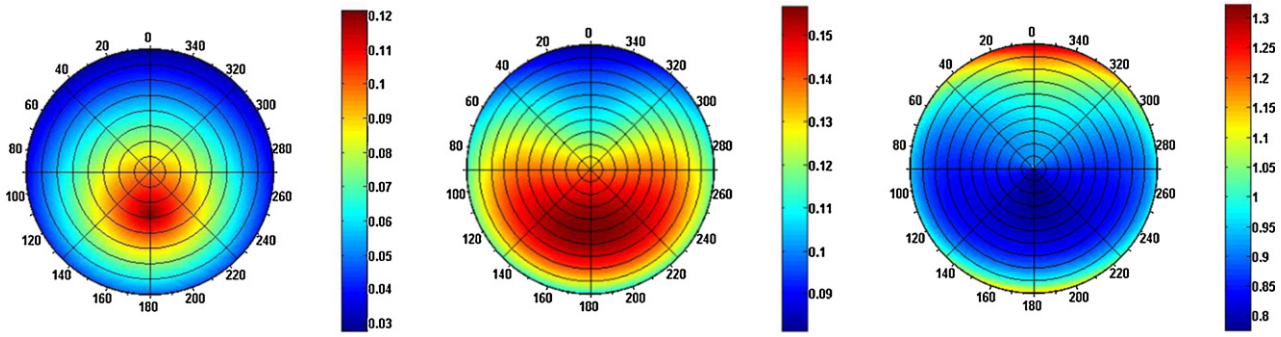

Fig. 10. Forward modelled hemispheric reflectance using inverted parameters from the [left] MRPV model on savannah data at SZA = 28°, [middle] RTLS model on savannah data at SZA = 28°, [right] RTLS model on snow data at SZA = 66°. Compare to reference data in Fig. 7-left and right.

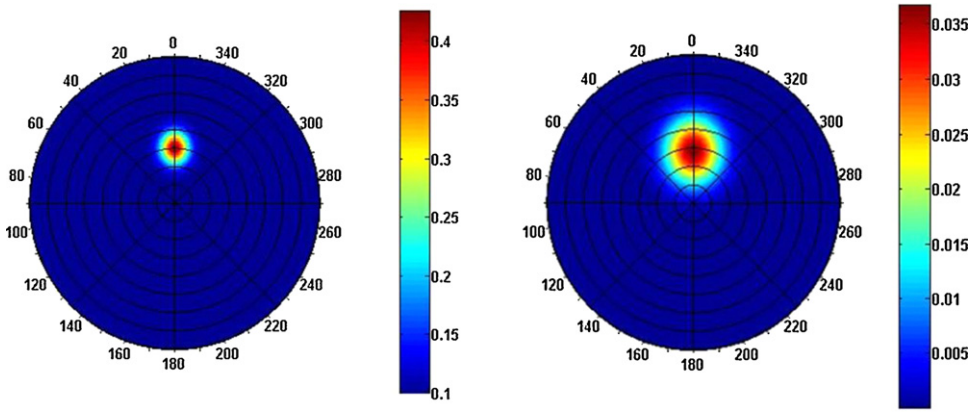

Fig. 11. Forward modelled hemispheric reflectance of water with the Cox–Munk model [Left] using inverted parameters when the model is fit to water BRDF data at SZA = 30°; [Right] using wind speed of 5 *m*/*s* and no sky radiance or aerosol depth. Compare to reference data in Fig. 6-middle.

efficiency (Nag, 2015). Genetic algorithms does equally well as simulated annealing but takes 4 times more time. Swarm optimization performed as well and as efficiently as SA, and could also be used. Unlike gradient-based methods in a convex design space, heuristics are not guaranteed to find the true global optimal solution in a single objective problem, but should find many good solutions (De Weck et al., 2008). Since we are trying to look for better spreads than those provided by monoliths in a global space, heuristics is our best alternative since they are good at dealing with local optima without getting stuck while searching for the global optimum.

3. Results of BRDF dependence on key variables

We found that BRDF estimation is a complex problem that depends on many variables—wavelength, number of measurements, VZA, RAA and SZA spread of the measurements. To simplify the OSSE as much as possible for rapid architecture evaluation, BRDF estimation sensitivity with respect these variables are analyzed in the context of the OSSE, data and models introduced in Section 2. The analysis has been performed per surface type from Fig. 5 because of their geographical knowledge and the availability of BRDF data. While we recognize that BRDF is influenced by intrinsic properties of the reflecting surface, we assume that CAR BRDF for each surface is representative of the anisotropic pattern of the BRDFs within that surface type. Sensitivity analysis on MBSE side of the model, to streamline the variable space so that only the key variables are simulated, has been published (Nag et al., 2015a).

For any given reference data (constant surface type and SZA) and any given number of satellites, unconstrained optimization will be used to find the best and worst angular sampling on the VZA–RAA polar plot. Obviously, the astrodynamics and systems engineering constraints will not allow a perfect spread, however, the analysis can inform what to aim for and what to avoid. Heuristic optimization routines, specifically simulated annealing, have been found to be the best for the purpose and are used from MATLAB's Optimization Toolbox (Nag, 2015). After constraining the key design variables in the OSSE, the SysEng Model's outputs (satellite states and corresponding angular coverage) can be evaluated in terms of BRDF estimation uncertainty. The reduced-variable OSSE will then be applied to an architecture tradespace to differentiate their science performance.

3.1. Sensitivity to wavelength

The CAR data are available at all angles for 8 wavebands, with the band width in parenthesis: #1 = 0.340 μm (0.009 μm), #2 = 0.381 μm (0.006 μm), #3 = 0.472 μm (0.021 μm), #4 = 0.682 μm (0.022 μm), #5 = 0.870 μm (0.022 μm), #6 = 1.036 μm (0.022 μm), #7 = 1.219 μm (0.022 μm) and #8 = 1.273 μm (0.023 μm). The 6 other wavebands, collected using the CAR's filter wheel, have not been used in this study. If the angular dependence is very different per waveband, then a different measurement spread will be optimal for different wavebands, in spite of looking at the same surface or ground spot. This will entail fractionating the instrument or flying instruments that measure different parts of the spectrum on different physical entities—adding more complexity to the mission. On the other hand, if the angular dependence per waveband is similar, then the formation geometry can be optimized for any band and optimal performance at the other bands expected. The BRDF data as a function of VZA and RAA per surface type (thus per SZA) were cross-correlated among all pairs of wavebands and results from the least correlated 4 surface types plotted in Fig. 8. Only significant correlations ($p < 0.05$) have been considered.

Snow and croplands show very high correlation among all band pairs and the minimum Pearson coefficient (r^2) is 0.83 and 0.67, respectively. The red and NIR bands (#4 and higher), our spectral region of interest in snow and vegetation, show very high correlation. Water shows significantly high correlation among all band-pairs except between the UV and NIR bands (#1 and #2) because the sun glint is very weak in the UV bands. Water leaving radiance in the absence of glint can be well approximated by the same formation geometry that estimates glint or radiance, hence, the low coefficients in UV do not pose a design change requirement in angular acquisition. Savannahs show low correlation between the blue/UV and red/NIR bands. This is because the vegetation hotspot is much stronger in the red or NIR bands than in blue or UV; band #3 and below show less pronounced anisotropy than the others. As before, a formation that captures the pronounced anisotropy, apparent in the red bands, should be able to capture the weak hotspot, if at all present, for less vegetated regions in the visible bands. Furthermore, the data we use does not include atmospheric correction. Atmospheric aerosols have more significant effect in the UV and VIS bands than others, which could be the reasons for divergence in anisotropy. Bands with pronounced signatures and least aerosol effects are therefore best selections for formation geometry optimization.

The wavelength analysis indicates that it is sufficient for the OSSE to use only one but representative waveband for the process of selecting and evaluating the formation because the optimal angular sampling at one band implies an optimal angular sampling of the other. Payload fractionation is also not required. In keeping with the above results, the representative band for water was selected to be #3 because the water leaving radiance is best seen at the CAR blue band; for vegetated regions (savannah, forests, croplands) we use #5 because the hotspot is most pronounced and for snow we use #6 because of minimal aerosol effects while keeping the pronounced glint. Data at the selected wavelengths are plotted in Fig. 5.

3.2. Sensitivity to BRDF models

One among the available BRDF models has to be chosen to extrapolate reflectance as accurately as possible at a few angles to the full hemispherical reflectance (BRDF) over any surface type. For any given surface and a 'perfect' angular spread (Box 1 and 2 in Fig. 4), the goodness of a model can be judged by the RMS error of BRDF estimation (green box in Fig. 4) and by its inversion residual. The inversion residuals have to be significantly lower than the RMS errors for the evaluation method (Fig. 4) to be used at all so that the RMS errors can be attributed to model or angular sampling imperfections, rather than mathematical aberrations.

RTLS, when inverting for its 3 parameters, has residual norms <0.05% of the measured reflectance values. The residuals are completely independent of the initial conditions, being a perfectly linear model, and have very little dependence on the angular spread. MRPV has slightly higher residuals, which are very sensitive to initial conditions. The CM model inversion, being the most non-linear, is very sensitive to the initial conditions and moreover, converges to very inconsistent parameters (e.g. wind speed) for different initial conditions but equally diverse angular spreads. To mitigate this instability, the true CM parameters for the OSSE data sets in this study, as inverted using the full radiative transfer SHARM code and published Gatebe et al., 2005, are used as the initial conditions.

RMS estimation errors among models are hard to compare because the perfect angular spread is not known or unique. For each of the 4 land surface types with pronounced angular signatures, 100 Monte Carlo runs were simulated with random numbers of satellites between 3 and 8 and random (unconstrained) angular spreads with those satellites. The RMS error in BRDF estimation (green box in Fig. 4) obtained from the MC runs are plotted in Fig. 9 when the model used is RTLS (left) or MRPV (right). The distributions are mostly right-tailed, indicating that random angular spreads (unfortunately impossible to achieve astrodynamically) minimize errors. RTLS performs marginally better than MRPV. MRPV does well for some surface types and initial conditions. For example, Fig. 10 shows the reconstructed BRDF from 9 satellites in an A-Train configuration when the MRPV (left) vs. RTLS (middle) model is used. The data set on which the models are fitted/inverted is the Savannah vegetation in Fig. 7-left at SZA = 28°. The shape of the reconstruction is better for MRPV however the values are closer for RTLS, thus leveling it out in terms of RMS errors. When a similar reconstruction is attempted using snow data, RTLS performs better in terms of shape and intensity and the reconstructed BRDF

Table 2
BRDF RMS errors when using measurements simulated by 6 satellites in a leader-follower configuration flying over water with variable SZA and using the RTLS vs. the CM model with initial wind speed (V) and aerosol optical depth (AOD) as listed, and an initial sky radiance algorithmically calculated.

Solar zenith angle	RMS error (RTLS)	RMS error (CM)	CM initial conditions
16°	0.02	0.02	$V = 6.14\ m/s$, AOD = 0.43
20°	0.05	0.02	$V = 1.58\ m/s$, AOD = 0.19
30°	0.04	0.02	$V = 1.08\ m/s$, AOD = 0.05
44°	0.05	0.04	$V = 2.88\ m/s$, AOD = 0.13

shown in Fig. 10-right. BRDF > 1 is due to normalization of aircraft collected data at the top of the atmosphere, and in keeping with the reference data in Fig. 7-right. This analysis along with RTLS's independence on initial conditions, linear form, lower residuals, NASA heritage in generating BRDF products and proven merit in both snow (Lyapustin et al., 2010) and vegetation (Román et al., 2011) led to the selection of RTLS as the land BRDF model on our OSSE.

The RTLS model when applied to water data gives very high errors compared to land data. The CM model, which depends strongly on wind speed, has traditionally been best suited for modeling water radiance (Gatebe et al., 2005; Gatebe et al., 2011). Measurements by a string of 6 satellites in the A-Train configuration at a random solar azimuth angle and 4 solar zenith angles corresponding to the CLAMS ocean BRDF data from CAR (Fig. 6 and Fig. 5-inset) were simulated. The RTLS and CM models were used on these datasets to invert for their respective parameters and the RMS errors between the forward model results and reference data in Table 2. The CM model performs better for most SZA angles compared to the RTLS, as expected, and will be used as the model in Box 4 of Fig. 4 whenever the simulated formation in Box 2 is expected to fly over water. For all other surface types, RTLS will be used.

The CM model's initial parameters, as mentioned before, are selected from the published values in (Gatebe et al., 2005), either from full SHARM inversions or measurements at the campaign site. The initial wind speed and aerosol optical depth per data set (sorted by SZA) are listed in Table 2. The initial sky radiance has been calculated by subtracting the BRDF term calculated using initial V and AOD from (Gatebe et al., 2005). Fig. 11-left shows the BRDF reconstructed from 6 measurements in a string of pearls configuration, like A-Train, using the CM model with the appropriate initial parameters applied to CLAMS data set for SZA = 30° (Fig. 6-middle). The reconstruction is accurate in terms of shape and intensity of the anisotropy, with inverted wind speeds $\sim 1\ m/s$. In contrast, when wind speeds of $5\ m/s$ and no aerosols or sky radiance were used, the BDRF signature is shown in Fig. 11-right. Radiance from water decreases with increasing wind speed (Feldman et al., 2011; Gatebe et al., 2005), decreasing aerosol concentration and increasing sky radiance. Wind speeds also spread out the sun glint size and for higher SZA angles (> = 50°) diffuse it along the principal plane.

3.3. Sensitivity to measurement angular spread

The next step is to estimate the optimal measurement spread in the VZA–RAA plane for a given SZA, satellite number and surface type. Heuristic optimization has been used for the purpose, specifically unconstrained simulated annealing. The SA algorithm included selecting an initial system temperature, initial spread and cooling schedule. We automated our temperature to $\text{abs}(-E_o/\log(0.99))$ where E_o is the BRDF error corresponding to the initial spread and selected a linear cooling schedule to allow for more time to converge. The objective function is the system energy (BRDF error), which needs to be minimized. Fig. 12 shows the results of SA optimization on an $N = 3$ point spread on the VZA–RAA plane for 4 different land surface types. The initial spread is a string of pearls/leader-follower/A-Train configuration with a random solar azimuth angle (red in all plots in Section 3). The final spread, irrespective of its shape, always moves away from the initial spread indicating that the initial configuration, which is the same as that obtained by all monoliths such as MISR and MODIS, is never optimal. The right-hand column shows the convergence history of the RMS errors (system energy or the objective function) from the initial spread to the final spread. Each history has one panel for the last re-arrangement (bottom) and the best-performing re-arrangement (top) per iteration. Convergence is confirmed because there is not much improvement in errors when the iterations were increased from 100 to 200.

Fig. 12 makes it obvious that the error improvement over the straight line spread is not equally significant for all surface types. The savannahs show the least error after convergence (0.013 or a 3.5% improvement), followed by water (0.022 or a 5% improvement) and croplands (0.054 or an 18.5% improvement), and finally snow (0.061 or a 20% improvement). Water has the lowest absolute value because the wavelength of the reference data used in the OSSE is lower than that of savannah, which is lower than croplands, and which is lower than snow. Hence, water (snow) data is expected to have the lowest (highest) absolute radiance. The cropland improvement is due to the initial spread being perpendicular to the principal plane, therefore missing the hotspot anisotropy entirely. The optimal spread pushes the sampling toward the hotspot (RAA = 180°, VZA = 68° as in Fig. 5 inset). The snow improvement similarly can be attributed to initial sampling missing the forward glint peak, which the optimal spread is able to capture (RAA = 0, VZA = 66° as in Fig. 7-right). This analysis demonstrates the importance of having a formation because monoliths are not always able to sample the top and bottom hemisphere of the BRDF polar plot due to the changing solar azimuth, and during these time periods, record higher than optimal BRDF errors. By spreading satellites over many azimuths, this under-sampling can be improved. In fact, even when the A-Train spread was able to sample both hemispheres (savannah and water in Fig. 12), spreading the measurements over the azimuth improved the errors by a few percentages. The optimization results of forests resemble that of croplands because of similar anisotropy and wavebands (Fig. 5-inset). Urban or city data has a very weak hotspot signature in the NIR bands and a very random angular signature in the visible bands due to high reflection off buildings, concrete and glass. Due to the relatively flat and random anisotropy plots of cities and deserts respectively, their formation optimization results are not as unique or customizable thus have not been shown.

3.4. Sensitivity to solar zenith angle

The previous section demonstrated the estimation benefit in spreading out angular measurements over zenith and azimuth for all the CAR datasets. CAR data has one solar zenith (SZA) per data set for most surface types. For data sets where multiple SZA are available, the effect of changing SZA is analyzed, to confirm the impact of its absence in some surface types. If BRDF estimation errors are sensitive to the CAR data's SZA, in spite of perfect SZA knowledge inputted into the models, then our current data will need to be supplemented with other BRDF data sources over and above CAR. For example, tower measurements from the AMSPEC instrument, which takes measurements at hundreds of SZA, can be used (Hilker et al., 2008; Nag et al., 2013). Fig. 7 shows the SZA dependence of land reflectance, primarily the position of the hotspot, and Fig. 6

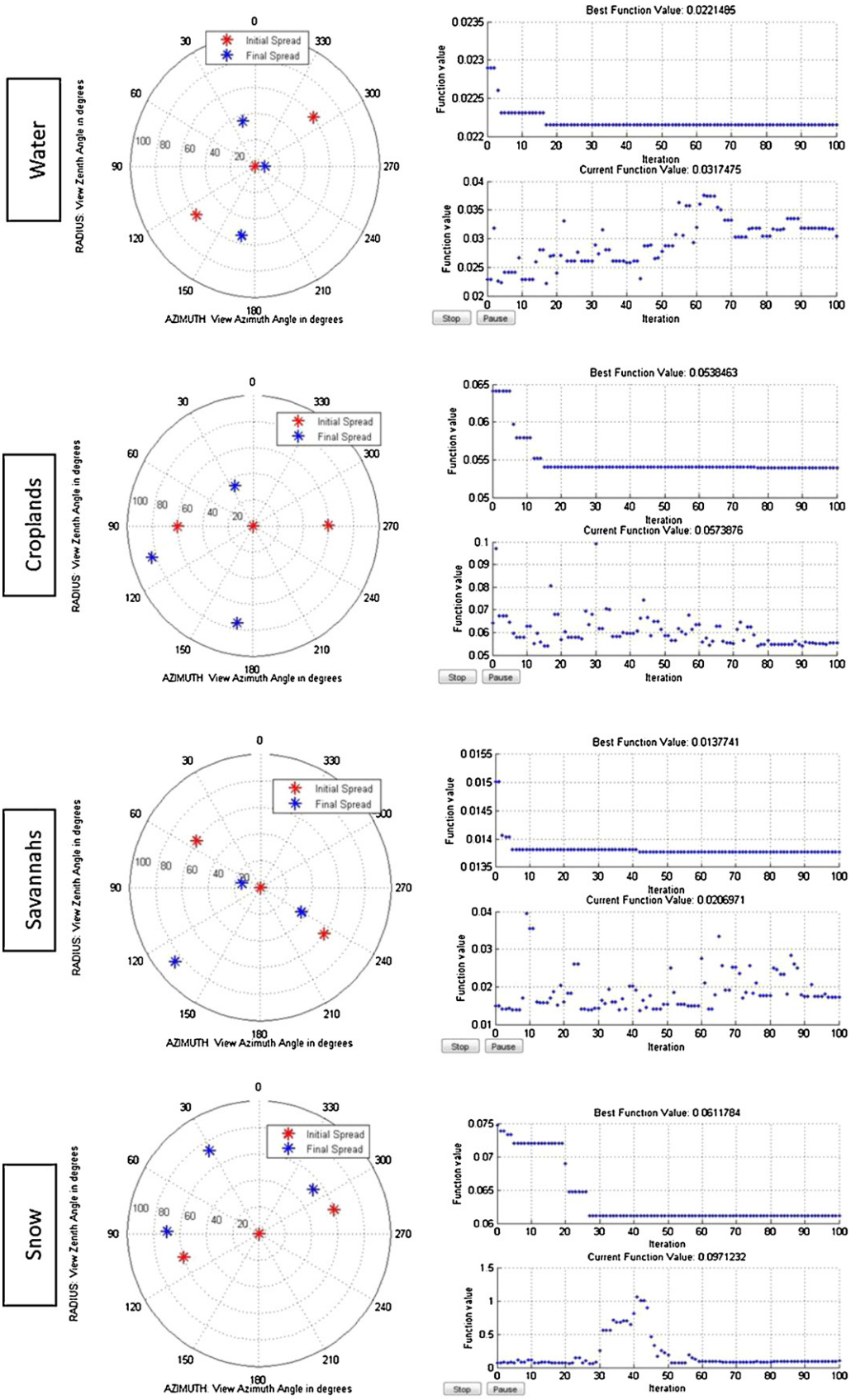

Fig. 12. Simulated annealing optimization results for 3-point measurements on the BRDF polar plot when inverting on data from the following surface types from top to bottom—water, croplands, savannahs, snow. The right-side column shows the convergence history of RMS errors from the initial to final spread. The radial striations for all angular spread plots are 20° in view zenith angle (VZA).

Table 3
BRDF errors associated with the initial and final spreads of 4-point measurements on the BRDF polar plot when inverting on CLAMS data for water BRDF at different SZA.

Solar zenith angle	Initial RMS error	Final RMS error
6°	0.0218	0.0172
20°	0.0303	0.0218
30°	0.0277	0.024
44°	0.0491	0.0373

Table 4
BRDF errors associated with the initial and final spreads of 4- and 6- point measurements on the BRDF polar plot when inverting on CLASIC, SAFARI and CLAMS data for 3 different surface types.

Surface type	$N=4$		$N=6$	
	Initial RMS error	Final RMS error	Initial RMS error	Final RMS error
Croplands	0.0773	0.0606	0.203	0.054
Savannah	0.019	0.014	0.026	0.013
Water	0.0277	0.024	0.0281	0.021

SZA dependence of water reflectance, primarily the position of the sun glint.

The positions of 4 points (corresponding to 4 unconstrained satellites) were optimized on the VZA–RAA polar plane for minimum BRDF error when selected from and fitted to water data from the CLAMS campaign. As before, these optimal spreads are impossible to maintain in a dynamic space orbit, and are only used to inform how the perfect spread changes as the solar illumination angle changes. Fig. 13 shows the resultant spreads from the optimization and Table 3 the corresponding BRDF errors. As expected, the optimal spreads move away from the initial A-train-like spread with a random solar azimuth because BRDF estimation is improved, to different extents for the different surface type, by azimuthal coverage. The improvement observed ~0.01 in absolute but ranges from 13 to 28% in the relative scale. Repeating the simulation using Savannah data at two SZAs shows similar significant improvement in error by adding more azimuthal spread but shows negligible error difference due to data sets with different SZA.

Neither the final VZA–RAA spreads nor their corresponding BRDF errors show a pattern with changing reference data as SZA changes (Fig. 6). A slight dependence can be gauged by the fact that the maximum VZA of the measurements increases as SZA increases, perhaps to be closer to the vicinity of the glint or hotspot. However, these spreads are in no way unique because similar low errors are possible by spreading out the 4 points in the different ways that capture more azimuth than zenith Table 4.

The key take-away is that the optimal angular spreads are not very sensitive to the SZA for the same surface type, when the SZA is known. While we acknowledge Helmholtz reciprocity and that optimal VZA is theoretically dependent on SZA, having precise knowledge of the SZA relaxes the stringency on the optimal VZA. Non-uniqueness of solutions is a shortcoming of heuristic optimization and its associated perturbation function to make different generations of variables. Nonetheless, heuristics does inform us that as long as angular measurements are available and well-spread on both hemispheres of the BRDF polar plot, the BRDF models are able to reconstruct the reference data with similar accuracy because they are able to predict the shape and size of the hotspot/glint based on the slopes around these features Fig. 13. A mission that produces greater coverage of the angular space can help improve these models and more accurate BRDF can be reconstructed using sub-optimal data. Given our BRDF models, CAR data classified using the MODIS land cover map, is deemed sufficient as reference data for our OSSE.

3.5. Sensitivity to number of satellites

A previous study has shown that BRDF RMS errors (estimation accuracy) do not depend on the number of measurements or satellites (Nag et al., 2014), for more than 3 view angles, and if arranged optimally for the Savannahs. This is expected because RTLS is a linear model with 3 parameters and should be uniquely invertible for non-redundant data, hence the importance of good angular spread. The CM model for water, due to its non-linearity and dependence on the radiative transfer model, is expected to show improved results with better spread of data points on the VZA–RAA plane. In this study, due to the true initial conditions, those effects are not seen.

Fig. 14 shows the optimal spread for 4 (left column) and 6 (right column) measurement points on the VZA–RAA plot, SZA notwithstanding, when optimized for BRDF data over croplands, savannah and water. The corresponding errors are shown in Table 3. The convergence histories are similar to those in Fig. 12. The error improvement from 4 to 6 measurements is negligible compared to the improvement from initial to final spread, i.e. from azimuthal spread of the measurements. Fig. 14 further shows that while optimization for $N=4$ spreads the measurement points around the polar plot when started off as a straight line (A-train or monolithic arrangement), the final spread does not improve much from $N=4$ to $N=6$. More points end up clustering at similar positions on the plot. While this can be numerically prevented by constraining the degrees of separation in the variables during optimization, it still indicates that similar low errors are possible with lower number of measurements, given currently selected models.

In spite of the negligible dependence of estimation errors on number of measurements, number of satellites is retained as a key variable in the OSSE for two reasons. One, the optimal spreads are impossible to maintain or achieve in the dynamic, orbital environment. While $N=3$ satellites may be sufficient for acceptable errors in the static, unconstrained frame, increasing the number of satellites increases the chances that one of the optimal spreads will be achieved in spite of the relative motion of the satellites and the disturbing forces (e.g. atmospheric drag) over their lifetimes (Nag, 2015; Nag et al., 2014). Two, the simple models (RTLS, MRPV, and CM) were designed to reconstruct BRDF from a few measurements that monolithic sensors are capable of providing. Better angular spread of measurements may not improve static BRDF estimation when used with the described models. However, better spread will certainly help the final products when radiative transfer models are used as well as pave the way for the design of more complex models such as those used in the fields of computer graphics and gravity estimation. This will help scientists understand the anisotropy of the observed surfaces.

4. Formation performance case study

The full architecture tradespace for varying angular samples is generated by varying the number of satellites between 3 (minimum required for BRDF models) and 8 (maximum constellation size funded by NASA (Yost, 2013) and choosing among the five most popular secondary launches from Spaceflight Inc.'s launch manifest.[3] The relative positions of satellites in a formation have been restricted to 8 slots with respect to the chief satellite, which

[3] Spaceflight Inc: http://spaceflightservices.com/manifest-schedule/.

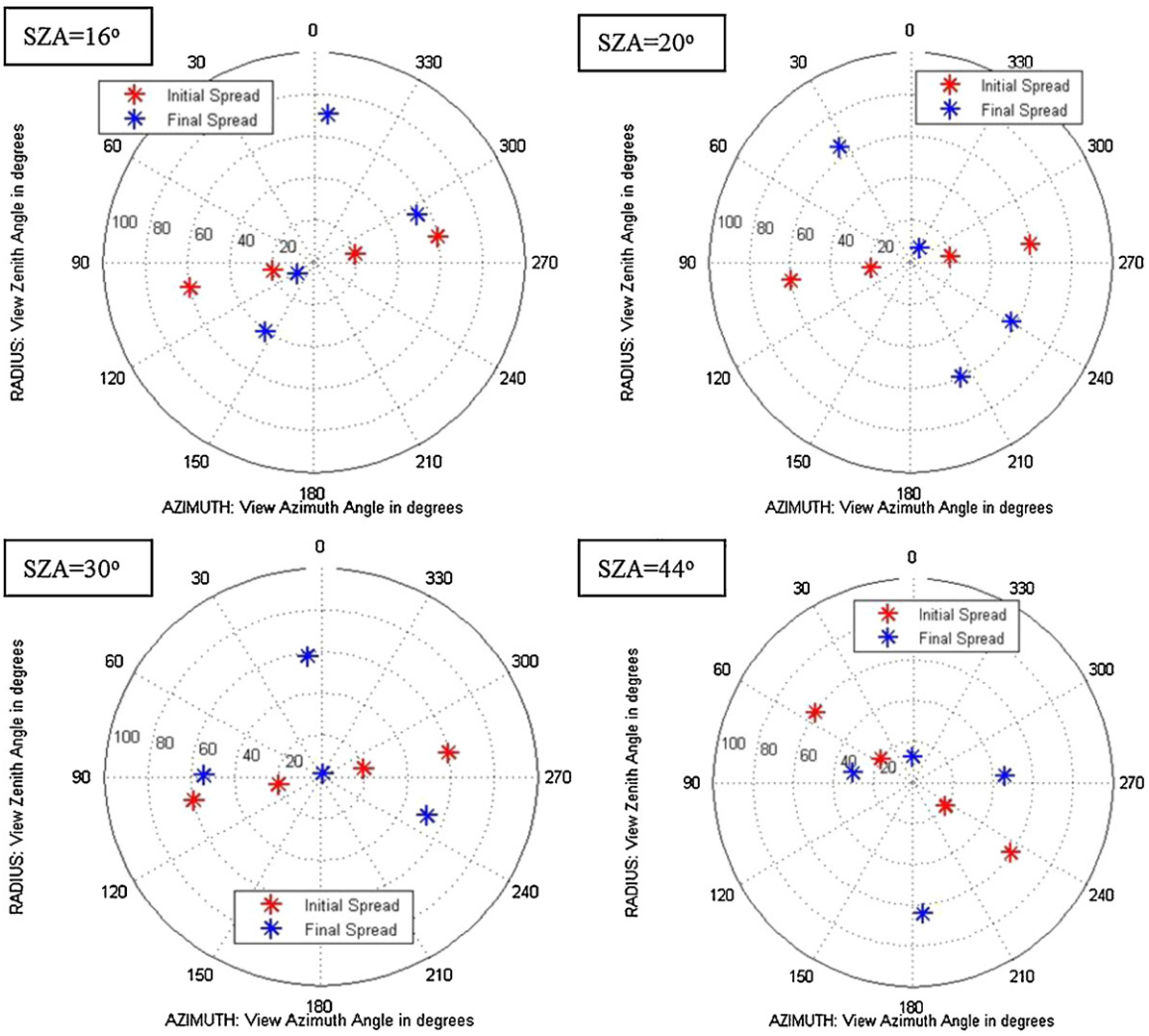

Fig. 13. Simulated annealing optimization results for 4-point measurements on the BRDF polar plot when inverting on CLAMS data for water BRDF at SZA = 16°, 20°, 30° and 44°. The radial striations for all angular spread plots are 20° in view zenith angle (VZA).

Table 5
Averaged percentages over a 4-h simulation with 154 maintainable formation configurations for only ISS chief orbit with variable number N of satellites. The numbers are for the configurations with minimum and maximum BRDF and albedo.

N = 6				*N* = 7				N=8			
BRDF		Albedo		BRDF		Albedo		BRDF		Albedo	
Min	Max	Min	Max	Min	Max	Min	Max	Min	Max	Min	Max
21.83	25.26	1.12	1.29	21.2	23.6	1.04	3.71	21.05	23.4	0.67	1.56

is the nadir-looking satellite. The only orbital elements that differentiate the slots are their right ascension of the ascending node and mean anomaly. While their relative positions with respect to the chief satellite change with time, orbit sensitivity studies (Nag et al., 2015a) have shown the selected 8 slots to be sufficient and maintainable using current, small satellite technology. They are shown as squares in Fig. 16-inset, and the presence of satellites in those slots as orange squares. For a given altitude and inclination of the chief orbit, there are a total of 1254 combinations to arrange 3–8 satellites into 8 slots (Nag et al., 2015a), which form the potential formation configurations.

Over the course of the orbit, the chief satellite changes periodically and all satellites point their payload dynamically toward the ground spot of the new chief satellite, so as to minimize the resultant BRDF error using an algorithm described in Reference (Nag, 2015) applied to the OSSE described in this paper. A Pareto frontier between performance and number of satellites in a formation can be seen in Fig. 15, for all possible configurations per satellite number. The ideal point is at the lower, left corner. Monolithic BRDF error is at 23.2%. Fig. 15 shows that 6 satellites, arranged optimally, can make angular measurements that estimate BRDF better than MISR can. To improve the error further at more cost, one can add additional satellites. The variance across configurations decreases with satellite number because of diminishing returns of organizing more satellites into a limited number of well-spread slots. The Pareto optimal formation configuration for any satellite number corresponds to that with the lowest average error percentage. The figure establishes that if the optimal configuration can be maintained, there is diminishing advantage to adding more than 6 satellites. However, in the event of inaccurate initialization or

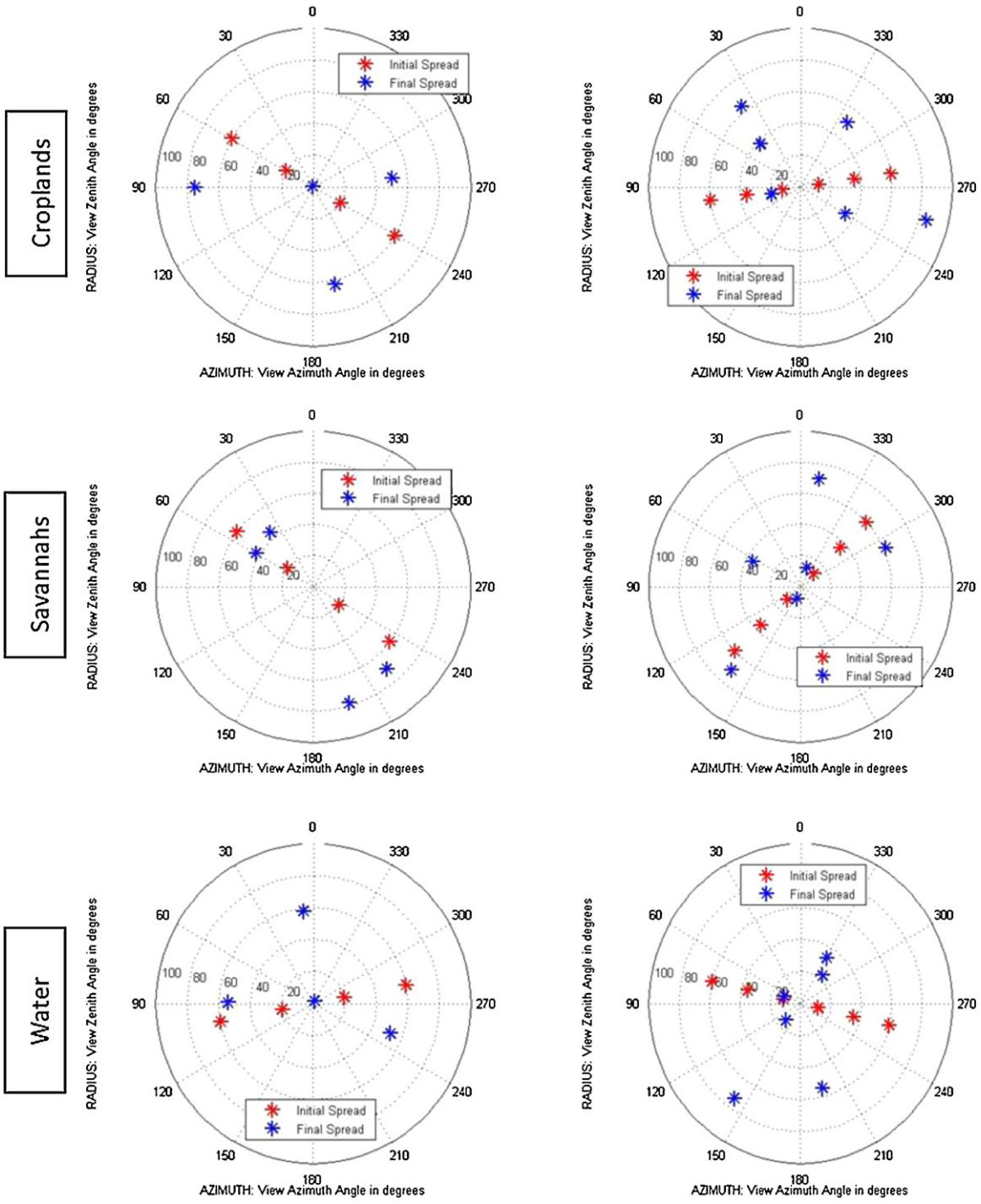

Fig. 14. Simulated annealing optimization results for 4 (left) and 6 (right)-point measurements on the BRDF polar plot when inverting on croplands, savannah and water data (from top to bottom). Plots can be compared to Fig. 12 for 3- point optimal spreads for the same surface type.

maintenance, there is slightly more advantage to having a larger number.

Fig. 16 shows the error curves over 93 min (one orbit only) for all formation configurations using 6 satellites for a chief orbit at 650 km, ISS inclination. Each configuration assumes a dynamically changing chief satellite that will point nadir while the others arrange their attitudes to point below it, using an imaging mode algorithm described in Reference (Nag, 2015) and the OSSE described in this paper. The BRDF error is calculated for every formation and MISR at every time step, using the method in Fig. 4 and the data from Fig. 5, depending on which surface type lies under the chief satellite. The time step is set to a minute, and can be made finer if a finer grid and spatial reference data distribution is used. The thick black line indicates the formation whose mean BRDF error over a 4 h period is the minimum (configuration shown as orange squares in Fig. 16-inset) and the black asterisks indicate the BRDF error due to MISR's measurements in a similar time period, calculated in the same way. While MISR does extremely well for much of the orbit, as expected because of its nine sensors well-spread in the zenith direction, it is outperformed by the formation for the section of the orbit when its sensors become perpendicular to the principal plane, causing major angular features

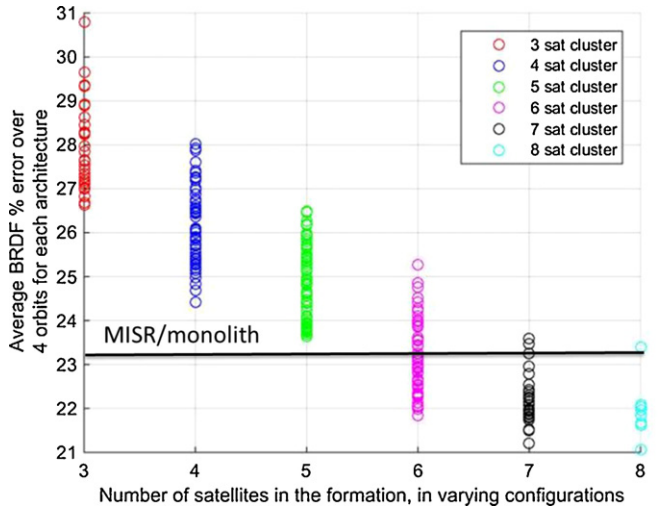

Fig. 15. Average estimation error over time for increasing satellite number at a 650 km, 51.6° orbit. Each circle represents a maintainable formation configuration. The horizontal black line represents MISR's estimation error, calculated in the same way (Fig. 4).

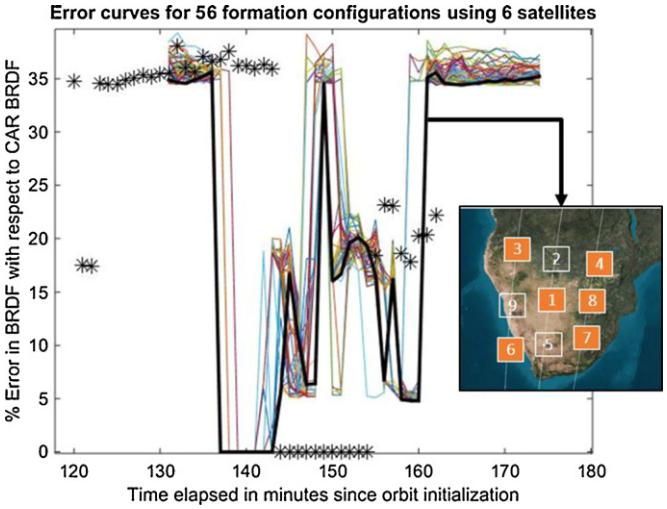

Fig. 16. BRDF error as a percentage of reference data over one orbit when a 6 satellite formation is simulated with a chief orbit of 650 km/51.6°, in all maintainable configurations (56), for one orbit. MISR error shown as asterisks and best performing formation error as thick, black line [Inset] Best formation configuration as orange squares with respect to nadir-pointing satellite (#1), arranged in 3 orbit planes.

to be under-sampled. The errors are plotted as percentages to prevent biases caused due to different surface types being sampled at the same time by MISR versus the formation (different orbits and time periods). The near-zero errors are over deserts because of their insignificant anisotropy, allowing a measurement at any one (known) angle to characterize BRDF. Fig. 16-inset serves as the proposed baseline that outperforms the monolith in angular sampling as well as other 6-satellite formations.

Table 5 shows the improved errors for both albedo and BRDF, assuming 6 to 8 satellites. While monolithic BRDF performance (23.2%) is matched well using 6 satellites, arranged optimally, the same feat can be achieved using 8 satellites arranged in any way. In the event of non-ideal initialization or maintenance of the formation and as long as they are spread in right ascension and mean anomaly, an 8-sat formation will outperform the monolithic configuration—thus making a strong case for flexibility and scalability of formation operations. More interestingly, the minimum albedo error percentage over all configurations for any number of satellites is better than MISR's error percentage of 3.6%. The ability to outperform monoliths for albedo with less satellites than those needed for BRDF can be attributed to the fact that albedo is a single value for any given spot. On the other hand, BRDF RMS error sums up the error for $360 \times 80 = 28{,}800$ different values of reflectance in different VZA and RAA directions, leaving more room for error compared to the reference data. Increasing the satellite number improves estimation errors for some extra dollars. Parallel literature (Nag, 2015) has also shown that the BRDF estimation errors calculated using the OSSE are independent of the chief orbit altitude and inclination, as long as the nadir-looking satellite can be changed dynamically to optimize the spread, thus providing launch flexibility for formation initialization. The coupled OSSE model enables informed choices for mission design based on the performance-cost Pareto front.

5. Summary

This paper describes an observing system simulation experiment (OSSE) to design and evaluate the performance of a small satellite formation for estimating BRDF via simultaneous multi-angular measurements. Current monolithic spaceborne instruments are not able to obtain such measurements due to being restricted in one orbital plane and end up compromising in other sampling dimensions to circumvent the planar restriction (Table 1). Airborne instruments, such as the CAR, provide excellent local data but cannot be used for global and frequent BRDF estimation. Current spaceborne and airborne data together make a state-of-the-art database for reference BRDF, based on which an OSSE can be built. Our overall tradespace analysis tool generates thousands of formation architectures which are then evaluated by the OSSE in terms of BRDF RMS error with respect to the reference data. The BRDF models selected are RTLS and MRPV for BRDF over different land surface types and Cox-Munk (CM) for water surfaces.

A rigorous study is performed to understand the dependence of BRDF estimation errors on key OSSE variables: wavelength of reflected light, BRDF models, solar zenith angle (SZA), measurement angular spread in terms of zenith angle (VZA) and azimuth angle with respect to the sun (RAA) and number of satellites. The RTLS model was found to be more consistent than MRPV for the purpose of this study due to its independence on initial conditions. Very precise initial conditions for the CM model were defined to prevent local trapping in its inherently non-linear inversion. Wavelength sensitivity showed that CAR BRDF data at wavelengths which display significant anisotropy are highly correlated, thus, the optimal angular spread of measurements at any of these wavelengths translates to an optimal spread at the others. SZA sensitivity showed that BRDF estimation errors do not depend on the SZA of the CAR data used as reference as long as the SZA value is precisely known, thus eliminating the need for denser datasets. VZA and RAA sampling sensitivity highlighted the importance of even, azimuthal sampling to reduce BRDF uncertainties but discounted the necessity of strict angular sampling requirements given the current BRDF models. Optimal angular spread is dependent on surface type and number of satellites but a well-spread sampling gave similar results over the full variable space. This inference is likely to change when complex models with integrated radiative transfer will be used to obtain the eventual ground products. Heuristic optimization (simulated annealing) was used to find the most optimal angular spreads, for specific values of OSSE variables. Satellite number was retained as an important OSSE variable to allow for flexibility in optimal angular spread as the relative positions of the satellites change with time and to provide measurements with better angular spread to build better BRDF models.

The OSSE model calculates BRDF errors per time step, as a function of the surface type below the satellite or formation, for all architectures of formations. MISR's configuration was selected as the monolithic state-of-art, because it provides the most accurate, global BRDF products. A formation of 6 satellites or more were found to produce lower BRDF estimation errors, averaged over multiple orbits, compared to the MISR configuration, when errors were calculated using the OSSE described in this paper. The OSSE allows the selection of the least error formation configuration as well as quantifies the performance improvement with increasing satellites and cost. All else being equal, the only error considered in this paper is that of angular sampling, therefore we make a strong case for formations serving as a complement to flagship missions in terms of such sampling gaps.

Future work includes refining the presented OSSE coupled with a systems engineering model to produce more rigorous error estimates. More generically, this work can serve as the introduction to a new method of mission design where in systems engineers, early in the design cycle itself, plug in their designs into appropriate OSSEs so that the science performance impact of their variable changes can be captured and traded. This process is all the more important for small satellites, constellations or any new measurement technique to prove science-quantifiable and justifiable addition to current flagship missions.

Acknowledgments

The authors acknowledge the following people, without whose help this paper in its present quality would not have been possible: Rajesh Poudyal (GSFC) for extracting and post-processing the BRDF data for the CAR instrument, Warren Wiscombe (GSFC) for his contribution and consistent drive toward Leonardo-BRDF which first proposed the concept of formation flight for BRDF, Ralph Kahn (GSFC), David Miller (MIT), Kerri Cahoy (MIT) and Alexei Lyapustin (GSFC) for their valuable ideas toward making this study better. The primary author is funded by the Schlumberger Faculty for the Future Fellowship and the NASA Earth and Space Science Fellowship.

References

Abrams, M., 2000. The Advanced Spaceborne Thermal Emission and Reflection Radiometer (ASTER): data products for the high spatial resolution imager on NASA's Terra platform. Int. J. Remote Sens. vol. 21 (5), 847–859.

Arnold, G.T., Tsay, S.-C., King, M.D., Li, J.Y., Soulen, P.F., 2002. Airborne spectral measurements of surface-atmosphere anisotropy for Arctic sea ice and tundra. Int. J. Remote Sens. vol 23 (18), 3763–3781.

Arnold Jr, C.P., Dey, C.H., 1986. Observing-systems simulation experiments: past, present, and future. Bull. Am. Meteorol. Soc. 67 (6), 687–695.

Barnsley, M.J., Strahler, A.H., Morris, K.P., Muller, J.P., 1994. "Sampling the surface bidirectional reflectance distribution function (BRDF): 1. Evaluation of current and future satellite sensors,". Remote Sens. Rev. vol. 8 (4), 271–311.

Barducci, A., Guzzi, D., Marcoionni, P., Pippi, I., 2005. CHRIS-Proba performance evaluation: signal-to-noise ratio, instrument efficiency and data quality from acquisitions over San Rossore (Italy) test site. In: Proceedings of the 3-rd ESA CHRIS/Proba Workshop, Italy.

Canadell, J.G., Quéré, C.L., Raupach, M.R., Field, C.B., Buitenhuis, E.T., Ciais, P., Conway, T.J., Gillett, N.P., Houghton, R.A., Marland, G., 2007. Contributions to accelerating atmospheric CO_2 growth from economic activity, carbon intensity, and efficiency of natural sinks. Proc. Natl. Acad. Sci. vol. 104 (November 47), 18866–18870.

Chopping, M., 2008. Terrestrial applications of multiangle remote sensing. Adv. Land Remote Sens. Syst. Model. Inversion Appl., 95–114.

Chopping, M., Su, L., Rango, A., Martonchik, J.V., Peters, D.P., Laliberte, A., 2008. Remote sensing of woody shrub cover in desert grasslands using MISR with a geometric-optical canopy reflectance model. Remote Sens. Environ. vol. 112 (1), 19–34.

Cox, C., Munk, W., 1954. Statistics of the sea surface derived from sun glitter. J. Mar. Res. 2, 198–227.

Crow, W.T., Chan, S.T.K., Entekhabi, D., Houser, P.R., Hsu, A.Y., Jackson, T.J., Njoku, E.G., O'Neill, P.E., Shi, J., Zhan, X., 2005. An observing system simulation experiment for Hydros radiometer-only soil moisture products. Geosci. Remote Sens. IEEE Trans. On vol.43 (6), 1289–1303.

Dyrud, L.P., La Tour, R., Swartz, W.H., Nag, S., Lorentz, S.R., Hilker, T., Wiscombe, W.J., Papadakis, S.J., 2014. The power of inexpensive satellite constellations. In SPIE Defense+ Security, 90832A.

Deschamps, P.Y., Bréon, M., Leroy, A., Podaire, A., Buriez, J.C., Seze, G., 1994. The POLDER mission: Instrument characteristics and scientific objective. Geosci. Remote Sens. IEEE vol. 32 (3), 598–615.

De Weck, O.L., Scialom, U., Siddiqi, A., 2008. Optimal reconfiguration of satellite constellations with the auction algorithm. Acta Astronaut. vol. 62 (2), 112–130.

Diner, D.J., Beckert, J.C., Reilly, T.H., Bruegge, C.J., Conel, J.E., Kahn, R.A., Martonchik, J.V., Ackerman, R., Gerstl, S.A.W., 1998. Multi-angle imaging spectroradiometer (MISR) instrument description and experiment overview. Geosci. Remote Sens. IEEE Trans vol. 36 (no. 4), 1072–1087.

Esper, J., Neeck, S., Wiscombe, W., Ryschkewitsch, M., Andary, J., 2000. Leonardo-BRDF: A New Generation Satellite Constellation, presented at the International Astronautical Conference , Rio de Janeiro, Brazil.

Feldman, D.R., Algieri, C.A., Ong, J.R., Collins, W.D., 2011. CLARREO shortwave observing system simulation experiments of the twenty-first century: simulator design and implementation. J. Geophys. Res. Atmos. 1984–2012 (116), D10.

Gatebe, C.K., King, M.D., Platnick, S., Arnold, G.T., Vermote, E.F., Schmidt, B., Jul, 2003. Airborne spectral measurements of surface-atmosphere anisotropy for several surfaces and ecosystems over southern Africa. J. Geophys. Res. 108 (D13), 8489.

Gatebe, C.K., King, M.D., Lyapustin, A.I., Arnold, G.T., Redemann, J., 2005. Airborne spectral measurements of ocean directional reflectance. J. Atmospheric Sci. vol. 62 (4), 1072–1092.

Gatebe, C.K., Wilcox, E., Poudyal, R., Wang, J., 2011. Effects of ship wakes on ocean brightness and radiative forcing over ocean. Geophys. Res. Lett. 38 (September 17).

Gatebe, C., Ichoku, C., Poudyal, R., Roman, M.O., Wilcox, E., 2014. Surface Albedo darkening from wildfires in Northern Sub-Saharan Africa. Environ. Res. Lett. 9 (June 13), http://dx.doi.org/10.1088/1748-9326/9/6/065003.

Godsalve, C., 1995. Bi-directional reflectance sampling by ATSR-2: a combined orbit and scan model. Remote Sens. vol. 16 (2), 269–300.

Hall, F.G., Hilker, T., Coops, N.C., Lyapustin, A., Huemmrich, K.F., Middleton, E., Margolis, H., Drolet, G., Black, T.A., 2008. Multi-angle remote sensing of forest light use efficiency by observing PRI variation with canopy shadow fraction. Remote Sens. Environ. vol. 112 (7), 3201–3211.

Hilker, T., Coops, N.C., Hall, F.G., Black, T.A., Wulder, M.A., Nesic, Z., Krishnan, P., 2008. Separating physiologically and directionally induced changes in PRI using BRDF models. Remote Sens. Environ. vol. 112 (6), 2777–2788.

Hilker, T., Coops, N.C., Hall, F.G., Nichol, C.J., Lyapustin, A., Black, T.A., Wulder, M.A., Leuning, R., Barr, A., Hollinger, D.Y., Munger, B., Tucker, C.J., 2011. Inferring terrestrial photosynthetic light use efficiency of temperate ecosystems from space. J. Geophys. Res. Biogeoscie. vol. 116 (G3).

King, M.D., Strange, M., Leone, P., Blaine, L., 1986. Multiwavelength scanning radiometer for airborne measurements of scattered radiation within clouds. J. Atmos. Ocean. Technol. vol. 3, 513–522.

Liang, S., 2008. Advances in Land Remote Sensing: System, Modelling, Inversion and Application. Springer.

Loeb, N.G., Wielicki, B.A., Doelling, D.R., Smith, G.L., Keyes, D.F., Kato, S., Manalo-Smith, N., Wong, T., 2009. Toward optimal closure of the Earth's top-of-atmosphere radiation budget. J. Clim. vol 22 (3), 748–766.

Lyapustin, A., Gatebe, R., Kahn, R., Brandt, J., Redemann, P., King, M.D., Pedersen, C.A., Gerland, S., Poudyal, R., 2010. Analysis of snow bidirectional reflectance from ARCTAS Spring-2008 Campaig. Atmos. Chem. Phys. vol. 10 (9), 4359–4375.

Lucht, W., Lewis, P., 2000. Theoretical noise sensitivity of BRDF and albedo retrieval from the EOS-MODIS and MISR sensors with respect to angular sampling. Int. J. Remote Sens. vol. 21 (1), 81–98.

Martonchik, J.V., Diner, B., Verstraete, M.M., Myneni, R.B., Knyazikhin, Y., Gordon, H.R., 1998. Determination of land and ocean reflective, radiative, and biophysical properties using multiangle imaging. Geosci. Remote Sens. IEEE Trans. vol. 36 (4), 1266–1281.

Morton, D.C., Nagol, J., Carabajal, C.C., Rosette, J., Palace, M., Cook, B.D., Vermote, E.F., Harding, D.J., North, P.R., 2014. Amazon forests maintain consistent canopy structure and greenness during the dry season. Nature.

National Academy of Sciences, 2007. Earth Science and Applications from Space: National Imperatives for the Next Decade and Beyond. National Academy Press.

National Research Council, 2012. Earth Science and Applications from Space: A Midterm Assessment of NASA's Implementation of the Decadal Survey. National Academies Press.

Nag, S., Cahoy, K., de Weck, O., Gatebe, C., Pasquale, B., Georgiev, G., Hewagama, T., Aslam, S., 2013. Evaluation of Hyperspectral Snapshot Imagers onboard Nanosatellite Clusters for Multi-Angular Remote Sensing. In: Proceedings of the AIAA Space Conference, San Diego.

Nag, S., Gatebe, C.K., De Weck, O.L., 2014. Relative trajectories for multi-angular earth observation using science performance optimization, in IEEE Xplore. In: Aerospace Conference 2014, Big Sky, Montana, USA.

Nag, S., 2015. Design and Evaluation of Distributed Spacecraft Missions for Multi-Angular Earth Observation. Massachusetts Institute of Technology, Cambridge, Massachusetts, U.S.A.

Nag, S., LeMoigne, J., Miller, D.W., De Weck, O.L., 2015a. A Framework for Orbital Performance Evaluation in Distributed Space Missions for Earth Observation, in IEEE Xplore. In: Aerospace Conference 2015, Big Sky, Montana, USA.

Nicodemus, F.E., Richmond, J.C., Hsia, J.J., Ginsberg, I.W., Limperis, T., 1977. Geometric considerations and nomenclature for reflectance. U.S.A. Department of Commerce/National Bureau of Standards, NBS Monogr, pp. 1–52.
Rahman, H., Verstraete, M.M., Pinty, B., 1993. Coupled surface-atmosphere reflectance (CSAR) model 1. Model description and inversion on synthetic data. J. Geophys. Res. vol. 98 (D11), 20,779.
Privette, J.L., Eck, T.F., Deering, D.W., 1997. Estimating spectral albedo and nadir reflectance through inversion of simple BRDF models with AVHRR/MODIS-like data. J. Geophys. Res. vol. 102 (D24), 29529.
M.O. Roman, C.K. Gatebe, Y. Shuai, Z. Wang, F. Gao, J. Masek, C. B. Schaaf, Use of In Situ and Airborne Multiangle Data to Assess MODIS- and Landsat-based Estimates of Surface Albedo, 2012.
Román, M.O., Gatebe, C.K., Schaaf, C.B., Poudyal, R., Wang, Z., King, M.D., 2011. Variability in surface BRDF at different spatial scales (30 m–500 m) over a mixed agricultural landscape as retrieved from airborne and satellite spectral measurements. Remote Sens. Environ. vol. 115 (September 9), 2184–2203.
J.R. Shell, Bidirectional Reflectance: An Overview with Remote Sensing Applications & Measurement Recommendations, Rochester N.Y., 2004.
Skrobot, G., Coelho, R., 2012. "ELaNa–educational launch of nanosatellite: providing routine rideshareopportunities,". AIAAUSU Conf. Small Satell. (August).
Soulen, P.F., King, M.D., Tsay, S.-C., Arnold, G.T., Li, J.Y., 2000. Airborne spectral measurements of surface-atmosphere anisotropy during the SCAR-A, Kuwait oil fire, and TARFOX experiments. J. Geophys. Res. Atmospheres vol. 105 (D8), 10203–10218.
Turmon M.J., Block G.L., Green R.O., Hua H., Jacob J.C., Sobel H.R. Springer P.L., Zhang, Q. Observing System Simulation Experiment (OSSE) for the HyspIRI Spectrometer Mission, 2010.
Van der Werf, G.R., Morton, D.C., DeFries, R.S., Olivier, J.G., Kasibhatla, P.S., Jackson, R.B., Collatz, G.J., Randerson, J.T., 2009. CO_2 emissions from forest loss. Nat. Geosci. vol. 2 (11), 737–738.
Wanner, W., Li, X., Strahler, A.H., 1995. On the derivation of kernels for kernel-driven models of bidirectional reflectance. J. Geophys. Res. Atmos. vol. 100 (D10), 21077–21089.
Wielicki, B.A., Harrison, E.F., 1995. Mission to planet Earth: Role of clouds and radiation in climate. Bull. Am. Meteorol. Soc. vol 76 (11).
Wielicki, B.A., Barkstrom, B.R., Harrison, E.F., Lee, R.B., Smith, G.L., Cooper, J.E., 1996. Clouds and the earth's radiant energy system (CERES): an earth observing system experiment. Bull. Am. Meteorol. Soc. vol. 77 (5), 853–868.
Xiong, X., Wolfe, R., Barnes, W., Guenther, B., Vermote, E., Saleous, N., Salomonson, V., 2011. Terra and Aqua MODIS Design, Radiometry, and Geometry in Support of Land Remote Sensing. Land Remote Sens. Global Environ. Change., 133–164.
Yost, B., 2013. "EDSN-Edison Demonstration for SmallS at Networks Overview," presented at the Small SatelliteConference , Logan, Utah.